Application of deep learning for technological parameter optimization of laser shock peening of Ti-6Al-4V alloy

M. Verezhak, A. Vshivkov, M. Bartolomei, E. Gachegova
Institute of Continuous Media Mechanics of the Ural Branch of Russian Academy of Science (ICMM UB RAS), Russia
mixailverejack@yandex.ru, https://orcid.org/0000-0003-2278-9439
vshivkov.a@icmm.ru, https://orcid.org/0000-0002-7667-455X
bartolomei.m@icmm.ru, http://orcid.org/0009-0003-3193-7605
gachegova.e@icmm.ru, https://orcid.org/0000-0001-6849-9889

A. Mayer
Chelyabinsk State University (CSU), Russia
mayer@csu.ru, https://orcid.org/0000-0002-8765-6373

S. Swaroop
Vellore Institute of Technology, India
n.r.sathya.swaroop@gmail.com, https://orcid.org/0000-0001-9872-811X

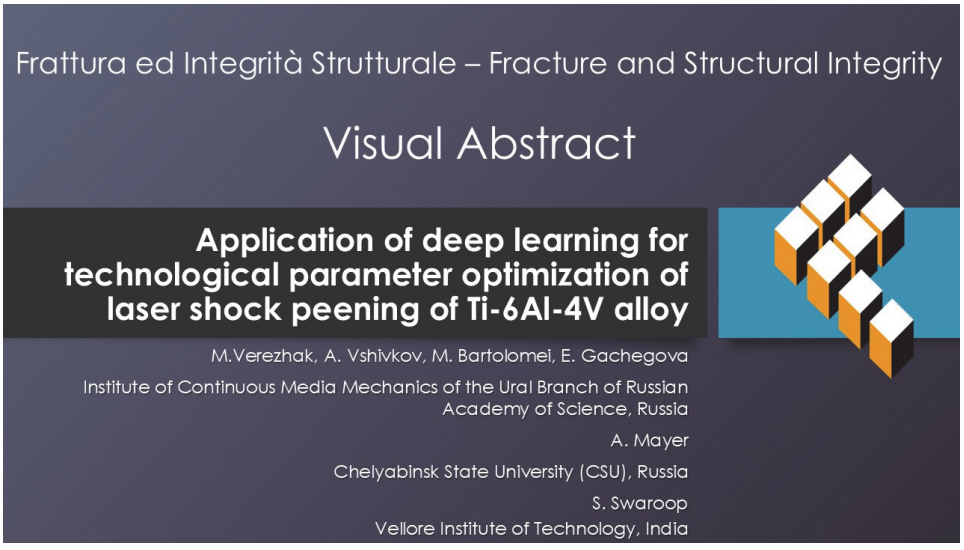

Citation: Verezhak, M., Vshivkov, A., Bartolomei, M., Gachegova, E., Mayer,A., Swaroop, S., Application of deep learning for technological parameter optimization of laser shock peening of Ti-6Al-4V alloy, Frattura ed Integrità Strutturale, 70 (2024) 121-132.

Received: 16.07.2024
Accepted: 07.08.2024
Published: 14.08.2024
Issue: 10.2024

KEYWORDS. Laser shock peening, Deep learning, Numerical simulation, Titanium alloy, Residual stress.

INTRODUCTION

Laser shock peening (LSP) [1-3] is an advanced technology that is used to introduce compressive residual stresses in surface layers of material. Residual stresses are formed due to the shock wave caused by high-energy laser pulses and significantly alter the fatigue properties of metallic materials and alloys. Unlike other laser methods LSP due to short (tens of nanoseconds) pulses allows to exclude heating of the surface layer of the material. The use of short laser pulses makes it possible to process parts of complex configuration and to obtain deeper residual stress fields compared to shot blasting, ultrasonic riveting or riveting with oil and water jets [12-15].

Compressive stresses resulting from laser exposure can compensate for existing or applied tensile stresses and prevent the appearance or propagation of fatigue cracks [16, 4]. However, in order to obtain an optimal residual stress distribution, it is necessary to properly select the pulse exposure parameters. In this connection, the inverse problem of determining the parameters of laser exposure according to the given residual stresses arises, which is relevant for the application of this technology.

The problem of finding the optimal parameters of laser shock peening of surfaces can be solved in several ways. One of the ways to solve this problem is the experimental selection of parameters with subsequent determination of residual stresses [17]. However, due to the limited and time-consuming nature of experiments, especially in the area of reliable determination of residual stresses, numerical modeling methods have become widespread.

Warren et al. conducted finite element modeling of LSP-induced residual stresses in carbon steel [5]. The authors performed 3D numerical simulations of single and multiple impacts in the Abaqus package using the custom VDLOAD subroutine to set the pulse amplitude. This allowed them to investigate the effects of spot size, location and pulse intensity on the magnitude of residual stresses. Various approaches to numerical modeling of laser impact peening have been proposed in [18, 19]. At present, simplified approaches using the eigenstrain method are traditionally used for modeling laser processing, which allow calculating a large number of laser impacts in an acceptable time [6].

The result of numerical modeling of the laser shock peening process is influenced by many parameters, in particular such values as the size and shape of the laser spot, profile and material model. The use of machine learning methods for predicting residual stresses caused by the LSP allows us to bypass the difficulties associated with modeling the process (solving the dynamic problem) of machining in each specific case.

Recently, the growth of computing power and the emergence of new algorithms opens up opportunities for the application of methods based on the big data processing. To solve complex problems in predicting mechanical properties, some authors use approaches based on machine learning, in particular with the help of neural networks [7,11,21]. Being one of the most important trend of artificial intelligence, artificial neural network (ANN) allows scientist to build a model that could solve complex prediction problems by imitating, in a sense, the behavior of network structures of the human brain [8]. For example, the authors of [9] applied this algorithm to predict the mechanical properties (roughness, microhardness and residual surface stresses) of stainless steel subjected to shot blasting. The results obtained showed that the correlation coefficient R^2 of experimental and validation data exceeded 0.99. In [10], a model for predicting residual stresses and hardness using ANN to optimize ultrasonic processing parameters was developed and it was shown that the predicted data agreed well with the experimental data.

Nevertheless, there are few works devoted to the application of the artificial neural network technique for predicting residual stresses after laser shock peening and determining the optimal impact parameters.

In this paper, a neural network model is developed to predict residual stresses and their penetration depth for titanium alloy *Ti-6Al-4V*. To train the model, a numerical-experimental method is implemented, which includes an experimental study of the effect of different modes of LSP on the depth and distribution of residual stresses. Based on the results of the experimental study, a numerical model is verified to simulate the process and prepare a database for training the ANN.

MATERIALS AND METHODS

Training dataset

Flat samples of titanium alloy *Ti-6Al-4V* with characteristic dimensions of *40x40x2mm* were used as a material for research. The chemical composition of the alloy is presented in Tab. 1 *(GOST 19807-91)*.

Results of *34* LSP experiments were used to train the artificial neural network and verify the model. The following parameters are the measured target characteristics: the residual stresses on the surface σ_{res}^{0}, the maximum compressive residual stresses in the surface layer $\sigma_{res}^{\max}$ and modified layer depth h .Distribution of residual stresses in depth after laser

shock peening were measured by hole drilling of experimental specimens. A characteristic plot of residual stress distribution in depth is shown in Fig. 1.

Ti	Al	V	Si	Fe	C	0	H
base	5.3 – 6.8	3.5 – 5.3	< 0.1	< 0.3	< 0.1	< 0.2	< 0.015

Table 1: Chemical composition of Ti-6Al-4V alloy (wt%).

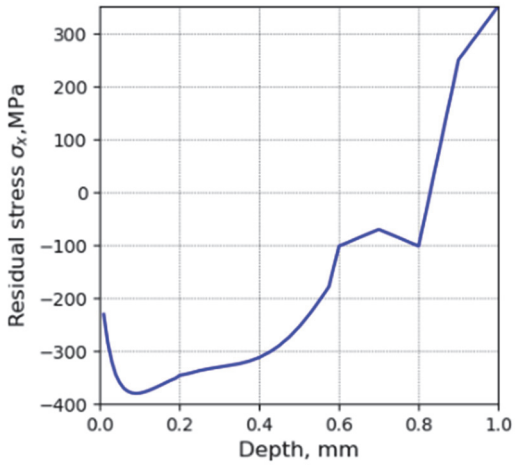

Figure 1: Distribution of residual stresses in Ti-6Al-4V after LSP with energy density of 20 GW/cm² after two pass.

Laser shock peening model and verification

In order to calculate residual stresses, an approach involving the solution of two coupled problems was used, similar to the idea proposed in [19]. The problem was solved in a three-dimensional formulation taking into account the finite size of the laser spot. At the first step, the dynamic problem of elastic-plastic wave propagation in the material was solved. The stress, strain, and displacement fields obtained during the dynamic explicit step are used as the initial conditions for the second step. At this step, a static equilibrium analysis is performed to determine the residual stress distribution. The component is not subjected external loading at this stage and the stress field is induced by the plastic strain that occurs in the dynamic step [22]. To conduct the static equilibrium analysis, the implicit solver is used that allows increasing the stability of the solving process. For the next laser shot, the results provided by the static analysis are transferred as initial conditions for the following dynamic step. To simulate laser irradiation, a pressure pulse was set at the target boundary in the impact region similarly to [16]. The stress-strain state induced by this loading is calculated in the finite element package Ansys LS-Dyna. To model the process of dynamic deformation of the material, the Johnson-Cook model was used as the governing relation. The analytical representation of the model is as follows:

$$\sigma_y = [A + B(\dot{\varepsilon}_{eq}^{pl})^n][1 + C\ln\frac{\dot{\varepsilon}_{eq}^{pl}}{\dot{\varepsilon}_{eq,o}^{pl}}][1 - \left(\frac{T - T_o}{T_m - T_o}\right)^m] \quad (1)$$

where σ_y – is the stress intensity at the yield surface, $\dot{\varepsilon}_{eq}^{pl}$ – is the plastic strain rate intensity, $\dot{\varepsilon}_{eq,o}^{pl}$ – is the reference plastic strain rate intensity, A, B, C, n – are parameters characterizing the inelastic behavior of the material, T – is the temperature of the material during the test, T_o – is the ambient temperature, T_m – is the melting temperature of the material, and parameter m is responsible for the thermal fracture.

Under the assumption that there is no thermal fracture as a result of lapping, temperature variables were not taken into account. The model parameters and mechanical constants are presented in Tabs. 2 and 3.

A, MPa	B, MPa	C	n	$\dot{\varepsilon}$
978	826	0.639	0.034	0.005

Table 2: Johnson-Cook hardening model constant for titanium alloy Ti-6Al-4V

ϱ, kg/m³	E, GPa	ν
4424	113	0.324

Table 3: Physical constants of titanium alloy Ti-6Al-4V

Numerical calculation for verification of the constructed mathematical model of residual stress generation process and finite element model are shown in Fig. 2. An area of 11x11*mm* with a 1x1*mm* square laser beam cross-section with a power density of 10 GW/cm^2 was treated. The energy of the pulse was *1 J*. For the considered energy parameters of exposure, the duration of the pressure pulse was 60 *ns* and the peak pressure value was *5.36 GPa*. No movement was allowed on the surface opposite the treatment area. The sides of the plate are free of load.
The mesh is tetragonal, the number of used elements is *149590*, the element size in the zone of pressure application did not exceed *0.2 mm*, a coarser mesh with a maximum finite element size of *2 mm* was formed at a distance from the load setting zone. The convergence of the solution was checked by mesh refinement.

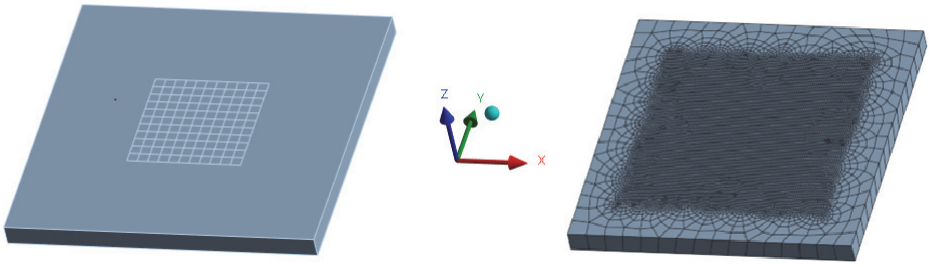

Figure 2: Numerical and finite-element model of alloy Ti-6Al-4V.

In order to verify the proposed model, the residual stress profiles obtained numerically were compared with experimental data. The residual stress profiles after LSP σ_x and σ_y , determined experimentally and numerically, are shown in Fig. *3*. The difference in minimum value of residual stress between experimental results and numerical results given in Fig. 3 is nearly 16%. This minor disagreement can be explained by possible measurement inaccuracies of the incremental hole drilling method due to its incremental and destructive character. A specific feature of the hole drilling method is the averaging of the obtained data over the drilled area. Therefore, it can affect the ability of it to register properly the above-described effect.

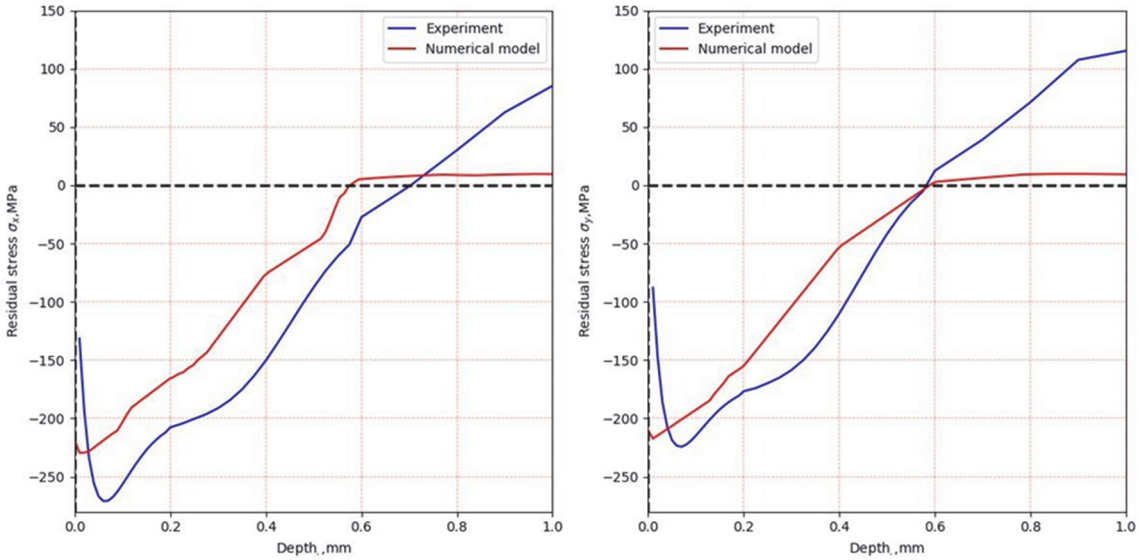

Figure 3: Residual stress profiles after LSP

The availability of a verified model significantly expands the possibilities of building a database sufficient for training a neural network and allows to significantly reduce the number of need experiments.

Formation on the training database

Three quantities were used as features for training the ANN model: beam overlap $f_{overlap}$, number of passes N_{pass} and density of embedded energy W. To account for the behavior of the model under small impacts, 6 objects $W=0$ with upon subsequent enumeration of N_{pass} and $f_{overlap}$ from the experimental value range. In this case, the target values for $h=0$, σ_{res}^{0} and $\sigma_{res}^{\max}$ were selected from measurements for the unprocessed surface of the alloy. The experimental database was complemented by the results of numerical modeling. The partitioning of the database was done in a *90/10* % ratio for the training and validation sample.

Architecture and training of neural network

We used a fully connected feed-forward propagation ANN as a machine learning model, the general structure of which is shown in Fig. *4*.

The ANN consists of *L+2* layers of neurons, where *L* is the number of hidden layers. The input layer receives the function arguments and the output layer generates the result of the network. We will number the layers with index *l*, running the values from *0* (input layer) to *L+1* (output layer).

When the ANN is triggered in the forward direction, the following calculations are performed layer by layer in all neurons of the hidden layers $l\in[1,L]$ and the output layer $l=L+1$ based on the "signals" (numbers) received from the artificial neurons of the previous layer:

$$X_k^{(l)} = f^{(l)}(z_k^{(l)}) \tag{2}$$

$$z_k^{(l)} = -b_k^{(l)} + \sum_{m=1}^{N_{l-1}} (a_{km}^{(l)} X_m^{(l-1)}) \tag{3}$$

where N_{l-1} are the number of neurons in the prior layer, $X_m^{(l-1)}$ are the signals of neurons of the prior layer, $a_{km}^{(l)}$ and $b_k^{(l)}$ are their weights and bias, respectively.

According to Eqn. (2), the intermediate result is formed first $z_k^{(l)}$ by linear combination of signals of the previous layer, then the nonlinear function from is calculated in Eqn. (1), the value of which gives the signal $X_k^{(l)}$ of this neuron and is fed to the next layer. In the case of the output layer, signals $X_k^{(l+1)}$ form output of the ANN.

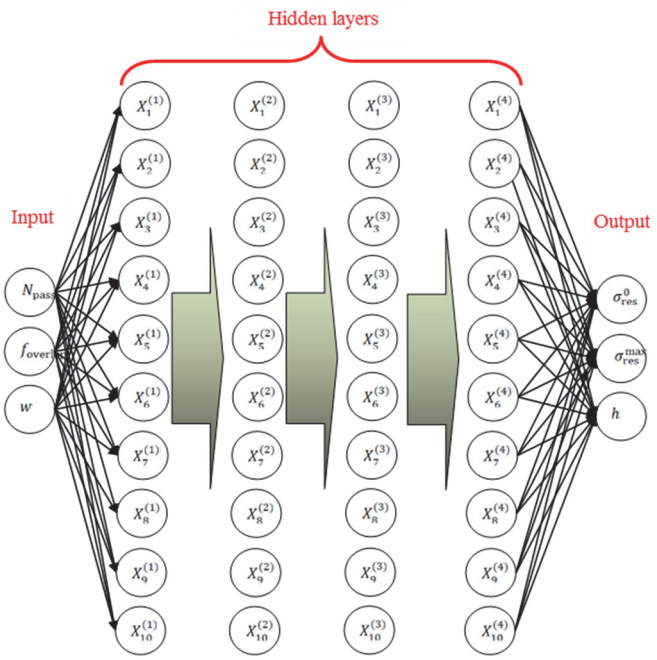

Figure 4: ANN structure for residual stress prediction.

A sigmoid transfer function was used for the output layer. All hidden layers of the neural network have the same functional form of transfer functions, which was one of the following 4 mappings: sin(z), Leaky ReLU, Swish or Sigmoid. The optimal of the mappings was used to verify the resulting deep learning model. The class of functions is represented as the following analytical expressions in the Tab. 4.

Function	Representation
Sine	$f^{(l)}(z_k^{(l)}) = \sin(z_k^{(l)})$
Leaky ReLU	$f^{(l)}(z_k^{(l)}) = \begin{cases} z_k^{(l)}, & 0 \le z_k^{(l)} \\ 0.01 z_k^{(l)}, & z_k^{(l)} \le 0 \end{cases}$
Swish	$f^{(l)}(z_k^{(l)}) = \dfrac{z_k^{(l)}}{1+\exp(-z_k^{(l)})}$
Sigmoid	$f^{(l)}(z_k^{(l)}) = \dfrac{1}{1+\exp(-z_k^{(l)})}$

Table 4: Analytical representation of transfer functions.

Input vector $x = \left\{ N_{pass}; f_{overlap}; w \right\}$ and output vector $y = \left\{ \sigma_{res}^{o}; \sigma_{res}^{\max}; h \right\}$ of the ANN are normalized using MinMax:

$$(x,y)_k = \frac{(x,y)_k - (x,y)_k^{\mathrm{I}}}{(x,y)_k^{\mathrm{II}} - (x,y)_k^{\mathrm{I}}} \tag{4}$$

where $(x,y)_k^{I,II}$ are reduced values of minimal and maximal of the corresponding input and output quantities calculated as:

$$(x,y)_k^{\mathrm{I,II}} = (x,y)_k^{ave} \pm \Delta \tag{5}$$

$$\Delta = 1.1 \cdot \max\left(\left| (x,y)_k^{\max} - (x,y)_k^{ave} \right|, \left| (x,y)_k^{ave} - (x,y)_k^{\min} \right| \right) \tag{6}$$

,where $(x,y)_k^{\max,\min}$ are the true values minimum and maximum, $(x,y)_k^{ave}$ are average values of input and output variables calculated from the training dataset. Likewise to [21], the binary cross-entropy function was used as a loss function for training the neural network, the analytical representation of which is given by the following expression:

$$S = -\sum_{\beta \in B} \sum_{n=1}^{N_{L+1}} \left[y_n^{\beta} \cdot \ln\left(y_n^{ANN}\left(x^{\beta}\right) \right) + (1 - y_n^{\beta}) \cdot \ln\left(y_n^{ANN}\left(x^{\beta}\right) \right) \right] \tag{7}$$

where $y^{ANN}(x^{\beta})$ is the current prediction of the ANN basing on the input vector x^{β}.

The ANN model was trained using back propagation algorithm. In order to build the optimal model, 13 variants of ANN structures were investigated with 10 samples of ANN for each particular structure. From the trained ANN samples, the optimally designed structure was selected in terms of complexity and prediction accuracy. The root mean square errors calculated basing on 10 ANN samples were analyzed separately on training and validation data, as well as the maximum errors of the ANN.

RESULTS AND DISCUSSION

Optimization of ANN structure

In order to determine the optimal structure of the neural network, models were trained by varying the following basic characteristics of the neural network: the number of hidden layers *L*, the number of neurons in the hidden layer *N* and the transfer function of hidden layers. For each particular structure, 10 ANN samples were trained, which made it possible to estimate the average error values for a given ANN structure and their statistical spread. The training results of the different ANN structures are shown in Fig. 5.

It can be seen that the RMSE (root-mean-square error) of ANN depending on the number of hidden layer neurons on training and validation data falls sharply up to *N*=10, then it decreases significantly slower, which becomes disproportionate to the increase in complexity of ANN, i.e., the number of fitted parameters, which are weights and bias of neurons. The maximum error on the validation data, as well as on the training data, does not change significantly.

Having chosen *N=10* as the optimal number of neurons in a layer based on the data presented in Fig. 5(a), we further investigated the accuracy of ANN depending on the number of hidden layers. The results are shown in Fig. 5(b). It can be seen that the ANN with *L=1* gives a very large error on the training data. This error decreases rapidly with the increase of the number of layers up to *L=3*, and then decreases much slower. On the other hand, the error on the validation data decreases when the number of hidden layers increases up to L=4, after which it is almost unchanged considering the statistical variation for different ANN samples.

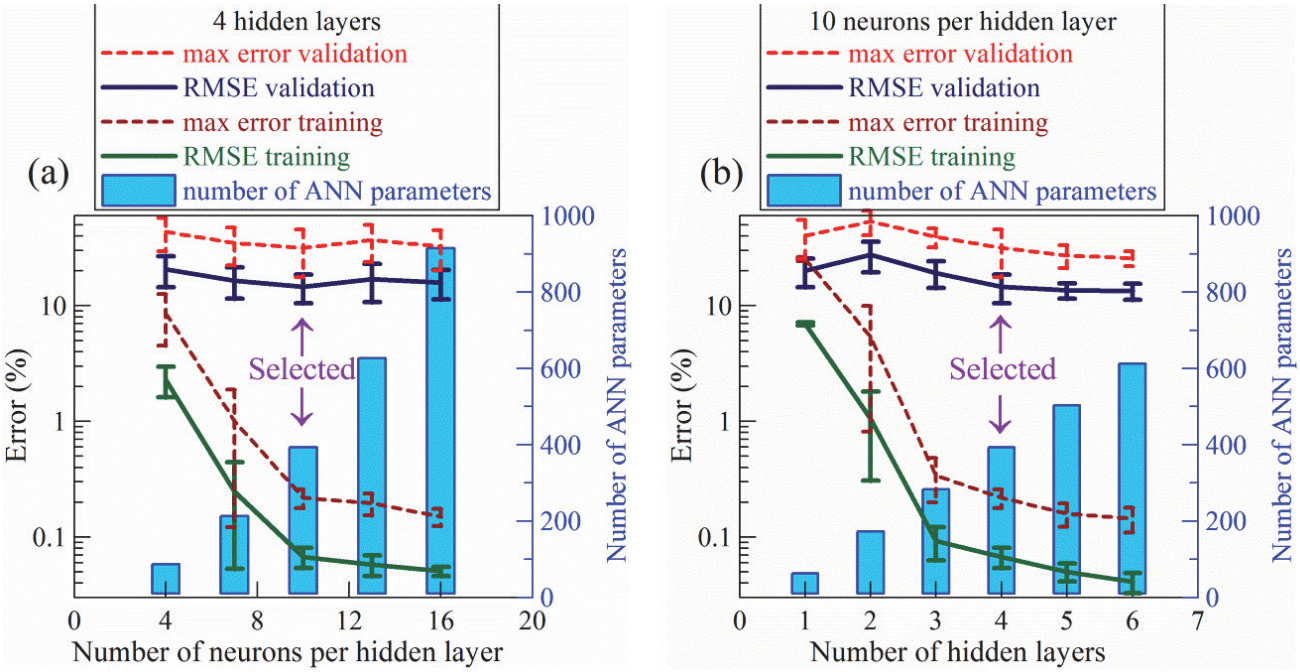

Figure 5: ANN error as a function of (a) the number of neurons in the hidden layer N and (b) the number of hidden layers L.

Based on the parametric studies carried out, a network with the number of hidden layers *L*=4 and the number of neurons in the layer *N*=10 was chosen as the main structure of the ANN. Investigation of the influence of the type of transfer function of the hidden layer neurons (Fig. 6) showed that the sin(x) function shows the minimum RMSE.

Verification of the ANN model of the LSP was carried out by calculating residual stresses and their penetration depth in titanium alloy *Ti-6Al-4V*. The values obtained were compared with validation data on which the network was not trained. The correlation curves on the training data (Fig.7) show a high degree of prediction, indicating the high accuracy of fitting the ANN to the data. The obtained ANN on validation data shows an acceptable value of accuracy. The best fit is obtained for the maximum residual stresses. The error in the quantitative calculation of surface stresses and residual layer penetration depth is much higher than for maximum residual stresses.

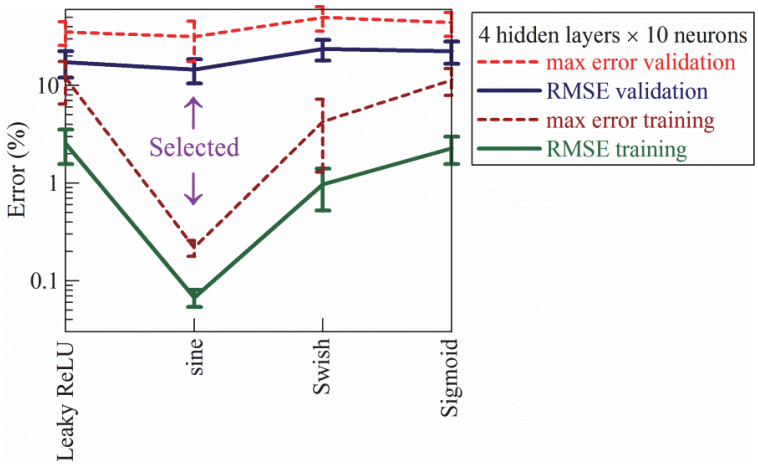

Figure 6: ANN error depending on the type of transfer function.

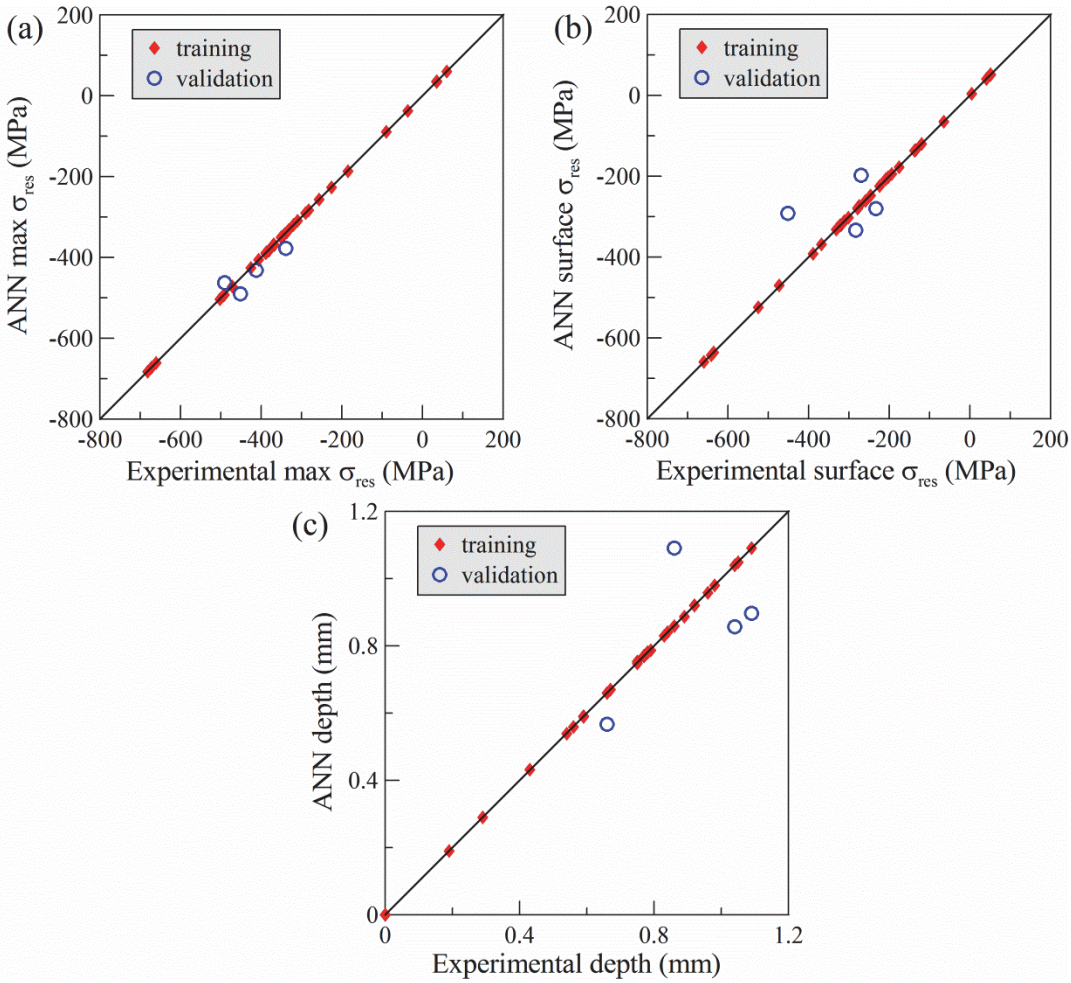

Figure 7: Correlation curves of ANN-predicted and measured values: (a) maximal compressive residual stresses, (b) surface residual stress and (c) depth of modified layer.

Selection of processing mode

The trained ANN is capable of describing the behavior of a numerical model or experimental results for predicting the hardened layer characteristics from laser shock peening parameters. The resulting deep learning model is used to optimize the plant parameters to obtain maximum residual layer depth and to generate maximum compressive residual stresses.

The distribution maps of the hardened layer depth h and maximum residual compressive stress σ_{res}^{max}, respectively, reconstructed using ANN are shown in Figs. 6 and 7. Each of the maps (Fig.8. and Fig.9.) are calculated by averaging 100000 ANN predictions.

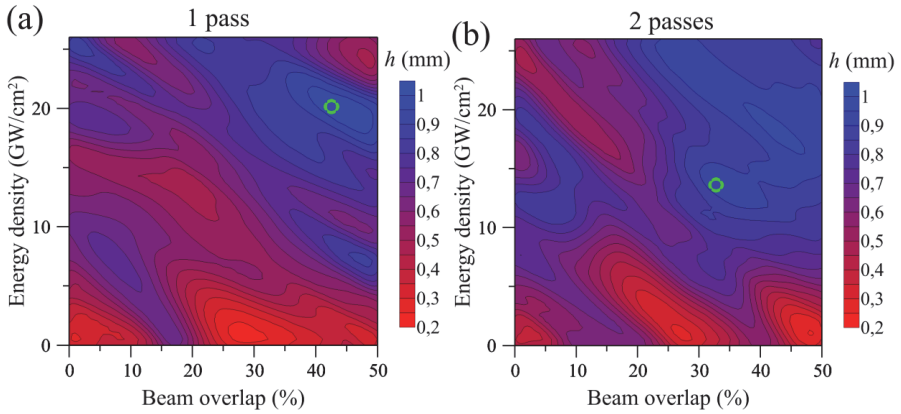

Figure 8: Maps of the modified layer depth distribution in the parameter plane for one (a) and two (b) passes, reconstructed using a trained ANN. Optimal parameter corresponding to the greatest depth at maximum compressive stresses not lower than -300 MPa are shown by green circles.

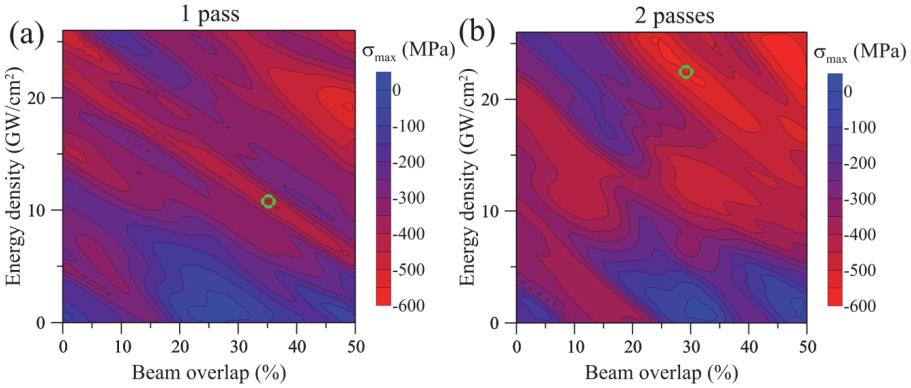

Figure 9: Distribution maps of maximum compressive stresses in the parameter plane for one (a) and two (b) passes, reconstructed using trained ANN. Optimal parameters corresponding to the highest compressive stresses at a modified layer depth of at least 0.5 mm are shown by green circles.

The generated maps show the possibility of interpolating data between training data points using the ANN. The distributions show the difficult dependence of the hardened layer depth and maximum compression stresses on the machining process parameters. The depth of the modified layer varies from 0.2 to 1.2 mm, while the range of compressive stresses changes from -600 MPa to 0 MPa.

We searched for optimal processing parameters to achieve: (1) the maximum depth of the hardened layer at compressive stresses σ_{res}^{max}; not lower than 300 MPa and (2) maximum compressive stresses at a modified layer depth of at least 0.5 mm. The calculated values of the optimal parameters are collected in Tab. 5 and shown in Figs. 8 and 9 (green circles).

Number of passes	Overlap (%)	Energy density (GW/cm²)	max σ_{res} (MPa)	Depth (mm)
1	35.2	10.8	-672	0.95
2	29.2	22.4	-683	1.05
1	42.5	20.1	-536	1.22
2	32.8	13.6	-598	1.18

Table 5: Optimal processing parameters determined using the ANN.

For engineering applications, in combination with optimum machining parameters and characteristic distribution maps similar to those shown in Figs. 8 and 9, it is important to know the permissible ranges of machining modes to ensure the

quality of the hardened layer is not lower than the threshold value. Fig. 10 shows the maps of allowable parameters calculated with the help of the ANN in comparison with the experimentally confirmed modes. It can be concluded that ANN prediction in that part is in full agreement with the experiment.

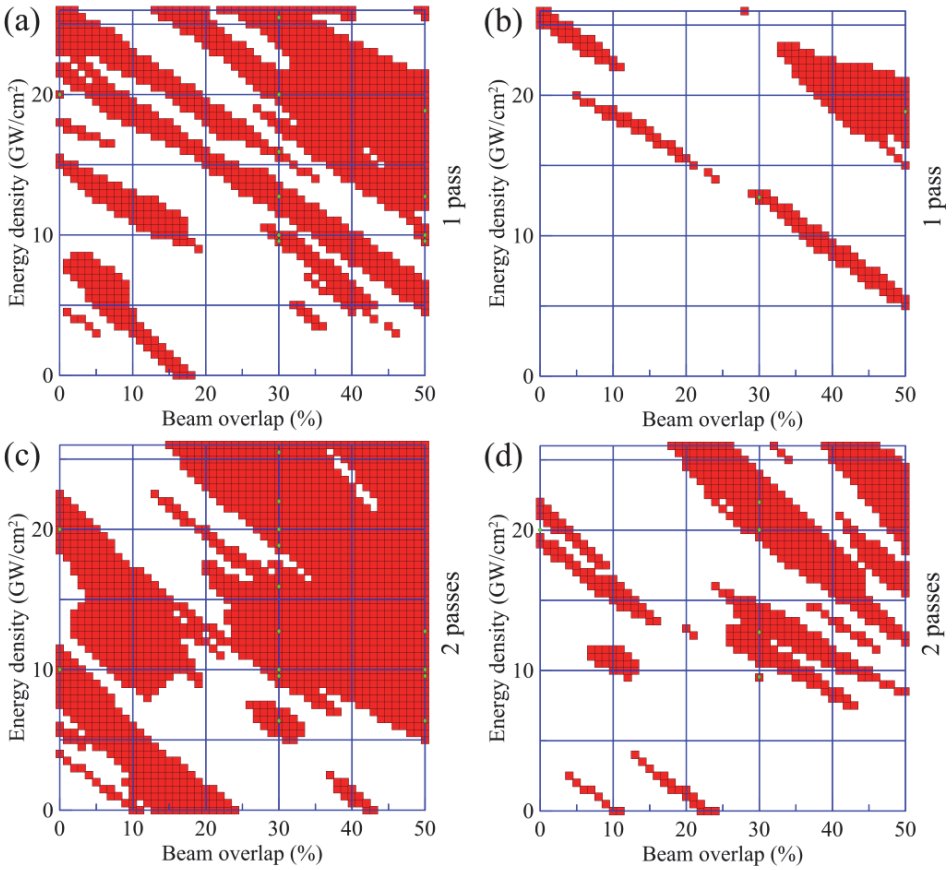

Figure 10: Processing modes leading to maximum compressive stresses in the surface layer of at least (a,c) -300 MPa and (b,d) -490 MPa and with a modified layer depth of at least (a,c) 0.5 mm and (b,d) 0.7 mm for (a,b) one pass and (c,d) two passes. Dark red squares show the ANN prediction, green rhombuses show the experimentally confirmed modes.

Conclusions

The study of the process of laser shock peening of samples manufactured from titanium alloy *Ti-6Al-4V* is carried out in this work. A new strategy for selecting the optimum peening parameters, providing the specified parameters of residual stresses, is proposed and realized on model specimens. The strategy is based on an original artificial neural network.

A laser shock peening model is implemented and validated to minimize the number of experiments required to train the neural network. As a result, the neural network was trained on a synthetic database including experimental and numerical results. The possibility of adding numerical experiments to the training database allows to increase its size for reliable training of the neural network. In this study, it was shown that the ANN structure with the number of hidden layers $L = 4$ and the number of neurons $N=10$ when using hidden sine layers as the transfer function shows the best accuracy for the problem at hand.

The developed artificial neural network can be used to interpolate the dependence between training points, as well as to search for optimal parameters or acceptable ranges of parameters of the processing process. The resulting model lets us effectively select the needed parameters of laser exposure according to the given limitations of values and depth of residual stresses. For selection of irradiation parameters for details of an arbitrary geometry, it is possible to do with a minimum set of experiments for verification of results of calculation of the mathematical model on a new geometry and to do a new database for training.

ACKNOWLEDGMENTS

The reported study was supported by the Government of Perm Krai, research project No. C-26/829. LSP treatment was carried out under financial support from the Programs for the creation and development of the world-class scientific center "Supersound" for 2020–2025 with the financial support of the Ministry of Education and Science of Russia (Agreement No. 075-15-2022-329 dated April 21, 2022).

REFERENCES

[1] Wu, J., Zhao, J., Qiao, H., Liu, X., Zhang, Y. and Hu, T. (2018) Acoustic wave detection of laser shock peening, Opto-Electronic Advances, 1(9), pp. 1–5. DOI: 10.29026/oea.2018.180016.

[2] Wu, J., Zhao, J., Qiao.H, Hu, X. and Yang, Y. (2020) The new technologies developed from laser shock processing, Materials, 13(6). DOI: 10.3390/ma13061453.

[3] Tang, L., Jia, W. and Hu, J. (2018) An enhanced rapid plasma nitriding by laser shock peening, Materials Letters, 231, pp. 91–93. DOI: 10.1016/j.matlet.2018.08.010.

[4] Guo, W., Sun, R., Song, B., Zhu, Y., Li, F., Che, Z., Li, B., Guo, C., Liu, L. and Peng, P. (2018) Laser shock peening of laser additive manufactured Ti6Al4V titanium alloy, Surface and Coatings Technology, 349, pp. 503–510. DOI: 10.1016/j.surfcoat.2018.06.020.

[5] Warren, A.W., Guo, Y.B. and Chen, S.C. (2008) Massive parallel laser shock peening: Simulation, analysis, and validation, International Journal of Fatigue, 30(1), pp. 188–197. DOI: 10.1016/j.ijfatigue.2007.01.033.

[6] Coratella, S., Sticchi, M., Toparli, M., Fitzpatrick, M., Kashaev, N. (2015) Application of the eigenstrain approach to predict the residual stress distribution in laser shock peened AA7050-T7451 samples, Surface and Coatings Technology, 273(1), pp. 39–49. DOI: 10.1016/j.surfcoat.2015.03.026.

[7] Merayo, D., Rodríguez-Prieto, A. and Camacho, A.M. (2020) Prediction of mechanical properties by artificial neural networks to characterize the plastic behavior of aluminum alloys, Materials, 13(22), pp. 1–22. DOI: 10.3390/ma13225227.

[8] Sarkar, A. and Chakravartty, J.K. (2013) Prediction of flow stress in cadmium using constitutive equation and artificial neural network approach, Journal of Materials Engineering and Performance, 22(10), pp. 2982–2989. DOI:10.1007/s11665-013-0597-9.

[9] Sembiring, J.P.B.A., Amanov, A. and Pyun, Y.S. (2020) Artificial neural network-based prediction model of residual stress and hardness of nickel-based alloys for UNSM parameters optimization, Materials Today Communications, 25. DOI: 10.1016/j.mtcomm.2020.101391.

[10] Maleki, E. and Unal, O. (2021) Shot Peening Process Effects on Metallurgical and Mechanical Properties of 316 L Steel via: Experimental and Neural Network Modeling, Metals and Materials International, 27(2), pp. 262–276. DOI:10.1007/s12540-019-00448-3.

[11] Soundararajan, R., Arthanari, R. and Sivasankaran, S. (2017) Modeling and Analysis of Mechanical Properties of Aluminium Alloy (A413) Reinforced with Boron Carbide (B4C) Processed Through Squeeze Casting Process Using Artificial Neural Network Model and Statistical Technique, Materials Today: Proceedings. Elsevier Ltd, pp. 2008–2030. DOI: 10.1016/j.matpr.2017.02.047.

[12] Abdulstaar, M., Mhaede, M., Wollmann, M. and Wagner L. (2014) Investigating the effects of bulk and surface severe plastic deformation on the fatigue, corrosion behaviour and corrosion fatigue of AA5083, Surface and Coatings Technology, 254, pp. 244–251. DOI: 10.1016/j.surfcoat.2014.06.026.

[13] Xie, L., Wen. Y., Zhan, K.,Wang, L., Jiang, C. and Ji, V. (2016) Characterization on surface mechanical properties of Ti-6Al-4V after shot peening, Journal of Alloys and Compounds, 666, pp. 65–70. DOI:10.1016/j.jallcom.2016.01.119.

[14] Mordyuk, B.N., Karasevskaya, O.P. and Prokopenko, G.I. (2013) Structurally induced enhancement in corrosion resistance of Zr-2.5%Nb alloy in saline solution by applying ultrasonic impact peening, Materials Science and Engineering: A, 559, pp. 453–461. DOI:10.1016/j.msea.2012.08.125.

[15] Feng, Y., Hu, S., Wang, D. and Cui, L. (2016) Formation of short crack and its effect on fatigue properties of ultrasonic peening treatment 355 steel, Materials and Design, 89, pp. 507–515. DOI: 10.1016/j.matdes.2015.10.009.

[16] Zhelnin, M., Kostina, A., Iziumova, A., Vshivkov, A., Gachegova, E., Swaroop, S. and Plekhov O. (2023) Fatigue life investigation of notched TC4 specimens subjected to different patterns of laser shock peening, Frattura ed Integrita Strutturale, 17(65), pp. 100–111. DOI: 10.3221/IGF-ESIS.65.08.

[17] Vshivkov, A., Iziumova, A., Gachegova, E and Plekhov O. (2024) Structural and fatigue features of Ti64 alloy after different laser shock peening, Russian Physics Journal, 67(3), pp. 287-295. DOI: 10.1007/s11182-024-03120-5.
[18] Kostina, A., Zhelnin, M., Vedernikova, A., Bartolomei, M. and Swaroop, S. (2024) Finite-element simulation of residual stresses induced by laser shock peening in TC4 samples structurally similar to a turbine blade, Frattura ed Integrita Strutturale, 18(67), pp. 1–11. DOI: 10.3221/IGF-ESIS.67.01.
[19] Sakhvadze G.H., Pugachev M.S. and Sakhvadze G.G. (2020) Effect lase shock processing texnology on the propagation of cracks in metal, Modern problems of machine theory, №9, pp. 62-65. DOI: 10.26160/2307-342X-2020-9-62-65.
[20] Pogorelko, V., Mayer, A., Fomin, E. and Fedorov, E. (2024) Examination of machine learning method for identification of material model parameters, International Journal of Mechanical Sciences, 265. DOI: 10.1016/j.ijmecsci.2023.108912
[21] Sterjovski, Z., Nolan, D., Carpenter, K., Dunne, D. and Norrish, J. (2005) Artificial neural networks for modelling the mechanical properties of steels in various applications, Journal of Materials Processing Technology, 170(3), pp. 536–544. DOI: 10.1016/j.jmatprotec.2005.05.040.
[22] Keller, S., Chupakhin, S., Staron, P., Maawad, E., Kashaev, N. and Klusemann, B. (2018). Experimental and numerical investigation of residual stresses in laser shock peened AA2198, J. Mater. Process. Technol., 255, pp. 294-307. DOI: 10.1016/j.jmatprotec.2017.11.023.